POLARIMETRIC RADAR CROSSTALK REMOVAL DURING SPARSE IMAGE FORMATION

Julie Ann Jackson *

Dept. of Electrical and Computer Engineering
Air Force Institute of Technology
Wright-Patterson AFB, OH 45433

Forest Lee-Elkin

Consultant
Xenia, OH 45385

ABSTRACT

We extend previous work in sparsity-regularized radar imaging to the case of multiple, coupled polarization channels. We demonstrate the ability to extract key canonical polarization signatures while emphasizing spatial sparsity and removing channel crosstalk. When the crosstalk is known, measured data can be decoupled prior to sparse imaging. However, the proposed incorporation of channel crosstalk in the sparse imaging optimization is preferred, as it enables future research of cases when crosstalk is not invertible or is not known.

Index Terms— radar imaging, polarimetric SAR, crosstalk, sparse regularization

1. INTRODUCTION

Sparsity-driven synthetic aperture radar (SAR) imaging has received considerable attention in the last decade, since the results introduced in [1, 2] can be tied to compressive sensing techniques [3, 4]. While design of a compressive sampling method for radar remains an open problem [5], regularized imaging can be applied to any data set to enhance features of interest. Previous work in sparsity-regularized radar imaging has emphasized point features and smoothly-varying features [1, 2, 6–9] as well as features from various signal dictionaries [10–13]. However, there has been very little consideration of enhancing polarimetric features. In this paper, we extend [1, 2] to jointly enhance multiple polarization channels. Our method removes channel crosstalk, emphasizes spatial sparsity, and recovers polarization information vital to target recognition tasks.

Enforcing spatial sparsity during image formation removes noise, clutter, and point spread effects to enhance target visualization. Polarimetric signatures disambiguate and further characterize target type. Recent work in [14] performed large area land cover classification via matching pursuit, using incoherent spatially-averaged polarization covariance matrices and an over-complete dictionary, learned from training samples in the image. We are interested in polarimetric decomposition of scattering mechanisms for target recognition, such as, for example, the vehicle classification problem in [15]. Therefore, we consider complex-valued SAR images and reflectivities, as in [1, 2, 6–13]. Much of that previous work has considered only a single radar channel during sparse reconstruction. Joint enhancement of multiple, independently-collected radar channels is developed for multi-pass interferometric SAR in [9]. However, polarimetric SAR (PolSAR) channels are simultaneously collected on the same platform. Data dependencies in the form of channel crosstalk can occur. Polarimetric decomposition of simple, simulated scenes in [8] did not suffer degradation due to independent channel sparse regularization; however, joint enhancement is more appropriate to preserve polarimetric information during sparse regularization. Also, in [16, Ch. 7], it is assumed that each channel has the same sparsity support, and a mixed-norm multiple measurements vector problem is solved. However, polarization channels may not have the same sparsity support (e.g. dihedral or trihedral scattering with non-zero co-pol response and zero cross-pol response [17]). Therefore, we extend prior work [1, 2] to the case of multiple, dependent channels by stacking the polarization channels. Although, it is known that crosstalk can be perfectly corrected (in the noiseless case) if all four polarimetric channels are collected [18, 19], we incorporate the channel crosstalk matrix in the image formation operation during sparse regularization. Including crosstalk in the multi-channel sparse imaging approach enables future extension of this work to cases in which the crosstalk matrix is not invertible or is unknown and must also be estimated. Thus, this paper provides a framework and initial examples for the relatively unexplored area of sparse-regularized polarimetric radar image enhancement.

2. SAR OVERVIEW

A single channel SAR image provides a two dimensional map of a scene's reflectivity at the radar's radio frequency and polarization. Image coordinates are range and cross-range from the radar. Due to finite bandwidth and limited aperture extent, the image $\underline{\underline{\boldsymbol{y}}}_1$ depicts a scene's complex-valued reflectivity response $\underline{\underline{\boldsymbol{x}}}_1$ convolved with the radar imaging system's impulse response, or point spread, function $\underline{\underline{\boldsymbol{h}}}_1$. Including additive noise $\underline{\underline{\boldsymbol{n}}}_1$, the image is $\underline{\underline{\boldsymbol{y}}}_1 = \underline{\underline{\boldsymbol{x}}}_1 * \underline{\underline{\boldsymbol{h}}}_1 + \underline{\underline{\boldsymbol{n}}}_1$, where the double-underline denotes a matrix. Alternatively, SAR imaging can be written as a discrete linear system model [1, 2, 5]

$$\underline{\boldsymbol{y}}_1 = \underline{\underline{\boldsymbol{A}}}_1 \underline{\boldsymbol{x}}_1 + \underline{\boldsymbol{n}}_1 \tag{1}$$

where $\underline{\boldsymbol{y}}_1$, $\underline{\boldsymbol{x}}_1$, and $\underline{\boldsymbol{n}}_1$ are a vectorized forms of their corresponding matrices and $\underline{\underline{\boldsymbol{A}}}_1$ is the single channel image formation operator. In practice, images are typically formed from collected data via back-projection or polar format algorithms (PFA) [20]. Explicit formation of $\underline{\underline{\boldsymbol{A}}}_1$ is not straightforward; however, after pre-processing the data by interpolation onto a regular grid, $\underline{\underline{\boldsymbol{A}}}_1$ can be easily implemented as a series of (inverse and forward) discrete Fourier transforms, zero-padding/truncation, and phase correction operations.

3. POLARIMETRIC SAR IMAGING

Reflections from an object depend on the polarization of the incident radiation; scattering information from multiple polarizations assists

*The views expressed in this article are those of the authors and do not reflect the official policy or position of the U. S. Air Force, Dept. of Defense, or the U.S. Government. Approved for public release: #88ABW-2016-6494.

target characterization. Polarimetric SAR transmits/receives multiple polarizations and provides a reflectivity image for each transmit/receive polarization channel.

The discrete linear system SAR imaging model with M channels has the same form as (1). The unknown polarization channel reflectivities $\underline{\boldsymbol{x}}_1, \ldots, \underline{\boldsymbol{x}}_M$ are stacked into the multi-channel reflectivity vector $\underline{\boldsymbol{x}} = [\underline{\boldsymbol{x}}_1^T, \ldots, \underline{\boldsymbol{x}}_M^T]^T$. Likewise, channel measurements are stacked into the multi-channel observed image vector $\underline{\boldsymbol{y}} = [\underline{\boldsymbol{y}}_1^T, \ldots, \underline{\boldsymbol{y}}_M^T]^T$, and per channel additive noise vectors are stacked into $\underline{\boldsymbol{n}} = [\underline{\boldsymbol{n}}_1^T, \ldots, \underline{\boldsymbol{n}}_M^T]^T$.

Although radar designs attempt to isolate each polarization antenna, crosstalk between the M channels can occur, resulting in contaminated measurements on each channel [18, 19]. The unknown multi-channel reflectivity at the nth pixel location is the length M vector

$$\underline{\boldsymbol{s}}_n = \begin{bmatrix} \underline{\boldsymbol{x}}_n, & \underline{\boldsymbol{x}}_{N+n}, & \cdots, & \underline{\boldsymbol{x}}_{(M-1)N+n} \end{bmatrix}^T \tag{2}$$

where N is the number of pixel locations in a single channel of $\underline{\boldsymbol{y}}$. (For simplicity of discussion, we refer to points in the image $\underline{\boldsymbol{y}}$ and points in reflectivity $\underline{\boldsymbol{x}}$ as pixels; however, $\underline{\boldsymbol{x}}$ may be defined at the sub-pixel level.) The effect of channel crosstalk at the nth pixel is modeled by the crosstalk matrix $\underline{\underline{\boldsymbol{C}}}$ so that, at the nth pixel location, the radar observes the mixture $\underline{\underline{\boldsymbol{C}}}\,\underline{\boldsymbol{s}}_n$. The crosstalk matrix

$$\underline{\underline{\boldsymbol{C}}} = \begin{bmatrix} C_{11} & C_{12} & \ldots & C_{1M} \\ C_{21} & C_{22} & \ldots & C_{2M} \\ \vdots & \vdots & \ddots & \vdots \\ C_{M1} & C_{M2} & \ldots & C_{MM} \end{bmatrix} \tag{3}$$

contains coefficients specifying what mixture of the M pure channels is observed at each of the $1, \ldots, M$ contaminated channels.

The relation between the measured multi-channel image vector and the unknown reflectivity is

$$\begin{aligned} \underline{\boldsymbol{y}} &= \underline{\underline{\boldsymbol{A}}}_M \,(\underline{\underline{\boldsymbol{C}}} \otimes \underline{\underline{\boldsymbol{I}}}_N)\, \underline{\boldsymbol{x}} + \underline{\boldsymbol{n}} & (4) \\ &= (\underline{\underline{\boldsymbol{C}}} \otimes \underline{\underline{\boldsymbol{I}}}_N)\underline{\underline{\boldsymbol{A}}}_M \,\underline{\boldsymbol{x}} + \underline{\boldsymbol{n}} & (5) \end{aligned}$$

where $\otimes$ denotes the Kronecker product, $\underline{\underline{\boldsymbol{I}}}_N$ is an $N \times N$ identity matrix, and $\underline{\underline{\boldsymbol{A}}}_M$ is the multi-channel imaging matrix

$$\underline{\underline{\boldsymbol{A}}}_M = \begin{bmatrix} \underline{\underline{\boldsymbol{A}}}_1 & 0 & 0 & \ldots \\ 0 & \underline{\underline{\boldsymbol{A}}}_1 & 0 & \\ 0 & 0 & \underline{\underline{\boldsymbol{A}}}_1 & \\ \vdots & & & \ddots \end{bmatrix}. \tag{6}$$

Commutation of terms in (4)-(5) is possible due to the block diagonal structure of the matrices. Incorporating channel crosstalk in the imaging operator, we have

$$\underline{\underline{\boldsymbol{A}}} = (\underline{\underline{\boldsymbol{C}}} \otimes \underline{\underline{\boldsymbol{I}}}_N)\underline{\underline{\boldsymbol{A}}}_M = \begin{bmatrix} C_{11}\underline{\underline{\boldsymbol{A}}}_1 & C_{12}\underline{\underline{\boldsymbol{A}}}_1 & \ldots & C_{1M}\underline{\underline{\boldsymbol{A}}}_1 \\ C_{21}\underline{\underline{\boldsymbol{A}}}_1 & C_{22}\underline{\underline{\boldsymbol{A}}}_1 & \ldots & C_{2M}\underline{\underline{\boldsymbol{A}}}_1 \\ \vdots & \vdots & \ddots & \vdots \\ C_{M1}\underline{\underline{\boldsymbol{A}}}_1 & C_{M2}\underline{\underline{\boldsymbol{A}}}_1 & \ldots & C_{MM}\underline{\underline{\boldsymbol{A}}}_1 \end{bmatrix}, \tag{7}$$

so the multi-channel extension of (1) is

$$\underline{\boldsymbol{y}} = \underline{\underline{\boldsymbol{A}}}\,\underline{\boldsymbol{x}} + \underline{\boldsymbol{n}}. \tag{8}$$

If crosstalk is negligible, then $\underline{\underline{\boldsymbol{A}}} = \underline{\underline{\boldsymbol{A}}}_M$ simply results in the multi-channel equation (8) being a stacked version of the single channel equation (1).

Key target signature information can be obtained from the polarimetric image stack. An estimate $\hat{\underline{\boldsymbol{s}}}_n$ of the polarimetric reflectivity (2) at pixel location n can be decomposed as $\sum_{q=1}^{Q} b_q \underline{\boldsymbol{s}}_q$ into Q scattering coefficients b_q for mechanisms $\underline{\boldsymbol{s}}_q$ that aid in target recognition and scene interpretation [15, 17, 21, 22]. Examples of basic scattering types include volume scattering, double-bounce scattering, odd-bounce scattering, and helix scattering [21, 23]. Pauli or Krogager bases are often used and relate to the aforementioned scattering types [15, 17]. Pseudo-color radar images may be generated to visualize the polarization response of a scene by associating one color with each basis vector [17, 21].

For simplicity, in this work, we consider an orthogonal basis set comprised of just three canonical polarization response types: trihedral $\underline{\boldsymbol{s}}_{\text{tri}} = \frac{1}{\sqrt{2}}[1, 0, 0, 1]^T$, dihedral $\underline{\boldsymbol{s}}_{\text{dih}} = \frac{1}{\sqrt{2}}[1, 0, 0, -1]^T$, and cross-pol $\underline{\boldsymbol{s}}_{\text{cross}} = \frac{1}{\sqrt{2}}[0, 1, 1, 0]^T$, where the four channels correspond to linear–horizontal (H) and vertical (V)–transmit and receive polarization channels: HH, HV, VH, and VV, respectively. The responses are mapped to cyan, magenta, yellow (CMY) colors, respectively, for visualization purposes. The estimated CMY coefficients of pixel n with response $\hat{\underline{\boldsymbol{s}}}_n$ are

$$[\hat{C}, \hat{M}, \hat{Y}] = \left[\frac{|\hat{\underline{\boldsymbol{s}}}_n^T \underline{\boldsymbol{s}}_{\text{tri}}|}{|\hat{\underline{\boldsymbol{s}}}_n|}, \quad \frac{|\hat{\underline{\boldsymbol{s}}}_n^T \underline{\boldsymbol{s}}_{\text{dih}}|}{|\hat{\underline{\boldsymbol{s}}}_n|}, \quad \frac{|\hat{\underline{\boldsymbol{s}}}_n^T \underline{\boldsymbol{s}}_{\text{cross}}|}{|\hat{\underline{\boldsymbol{s}}}_n|} \right]. \tag{9}$$

Our image reconstruction method is not limited to three basis vectors; however, visualization becomes more difficult when mapping more than three basis vectors to a pseudo-color image. Estimated target polarization responses are displayed in Figure 4, where pure CMY colors represent each of the three basis vectors $\{\underline{\boldsymbol{s}}_{\text{tri}}, \underline{\boldsymbol{s}}_{\text{dih}}, \underline{\boldsymbol{s}}_{\text{cross}}\}$.

4. MULTI-CHANNEL SPARSE REGULARIZATION

Radar aperture and bandwidth limitations broaden the point spread function $\underline{\underline{\boldsymbol{h}}}$, resulting in target spreading in the image domain. When there are few scatterers compared to the scene size, spatially-sparse estimates of scene reflectivity that remove or reduce the point spreading may be recovered by solving [1, 2]

$$\arg\min_{\underline{\boldsymbol{x}}} \|\underline{\boldsymbol{y}} - \underline{\underline{\boldsymbol{A}}}\,\underline{\boldsymbol{x}}\|_2^2 + \lambda_1 \|\underline{\boldsymbol{x}}\|_p^p, \tag{10}$$

where λ_1 is a positive scalar that enforces sparsity, as measured by the p-norm of the estimated reflectivity function $\underline{\boldsymbol{x}}$, with $0 < p \leq 2$. For $1 \leq p \leq 2$ minimization of (10) is convex [1]. Smaller p or larger ℓ_p sparsity penalty coefficient λ_1 equate with increased solution sparsity. Previous work has considered a single independently-collected radar channel. We consider multiple, simultaneously-collected channels with crosstalk, defining $\underline{\boldsymbol{y}}$, $\underline{\underline{\boldsymbol{A}}}$, and $\underline{\boldsymbol{x}}$ as specified for (8).

Alternatively, if $\underline{\underline{\boldsymbol{C}}}$ is known and invertible, then one can preprocess the observed data $\underline{\boldsymbol{y}}$ and solve the sparse imaging problem

$$\arg\min_{\underline{\boldsymbol{x}}} \|(\underline{\underline{\boldsymbol{C}}} \otimes \underline{\underline{\boldsymbol{I}}}_N)^{-1}\underline{\boldsymbol{y}} - \underline{\underline{\boldsymbol{A}}}_M \,\underline{\boldsymbol{x}}\|_2^2 + \lambda_2 \|\underline{\boldsymbol{x}}\|_p^p. \tag{11}$$

We note that (11) is valid but is not equivalent to (10) because the ℓ_2-norm expression differs. Current theory does not characterize the intersection of the solution space of (10) (as a function of λ_1) and the solution space of (11) (as a function of λ_2), and that topic is beyond the scope of this current work. Furthermore, we do not consider the general problem of choosing an ℓ_p sparsity penalty coefficient, which is discussed for SAR imaging in [24].

Although both (10) and (11) yield sparse solutions $\underline{\boldsymbol{x}}$ that balance the ℓ_2 and ℓ_p error terms, we prefer the problem setup (10), where $\underline{\underline{\boldsymbol{A}}}$ includes crosstalk, as defined in (7). The optimization (10) decouples crosstalk during sparse image formation and may be easily extended to consider cases where $\underline{\underline{\boldsymbol{C}}}$ is not invertible or where components of $\underline{\underline{\boldsymbol{C}}}$ are unknown and must also be estimated, for example using bilinear optimization [25].

To solve (10), we follow the surrogate optimization approach in [2]. This is an iterative process where

$$\left[\underline{\underline{\boldsymbol{A}}}^H\underline{\underline{\boldsymbol{A}}} + \frac{\lambda}{2}\underline{\underline{\boldsymbol{D}}}(\underline{\boldsymbol{x}}^{(i)})\right]\underline{\boldsymbol{x}}^{(i+1)} = \underline{\underline{\boldsymbol{A}}}^H\underline{\boldsymbol{y}} \tag{12}$$

is solved for $\underline{\boldsymbol{x}}^{(i+1)}$ using a preconditioned conjugate gradient (PCG) [26] numerical search. Iteration index i is incremented, and the process is repeated until convergence criteria are satisfied, indicating that $\underline{\boldsymbol{x}}$ has reached a fixed point of (12) . (Note, to solve the alternative problem (11), the solution (12) is modified by replacing $\underline{\underline{\boldsymbol{A}}}$ with $\underline{\underline{\boldsymbol{A}}}_M$ and observations $\underline{\boldsymbol{y}}$ with the pre-processed data $(\underline{\underline{\boldsymbol{C}}} \otimes \underline{\underline{\boldsymbol{I}}}_N)^{-1}\underline{\boldsymbol{y}}$). In (12),

$$\underline{\underline{\boldsymbol{D}}}(\underline{\boldsymbol{x}}^{(i)}) = \begin{bmatrix} p(|\underline{\boldsymbol{x}}_1^{(i)}|^2+\epsilon)^{p/2-1} & 0 & 0 \\ 0 & \ddots & 0 \\ 0 & 0 & p(|\underline{\boldsymbol{x}}_N^{(i)}|^2+\epsilon)^{p/2-1} \end{bmatrix} \tag{13}$$

where each entry is, for some small ϵ, an approximation to the ℓ_p-norm for purposes of differentiability [2]. Also, following [1, 2], we do not explicitly form $\underline{\underline{\boldsymbol{A}}}$ (or $\underline{\underline{\boldsymbol{A}}}_M$) but use more computationally efficient strategies.

5. RESULTS

We generate an example scene of four targets comprised of ideal point scatterers endowed with trihedral, dihedral, or cross-pol responses. The target point scatterer locations, amplitudes, and ideal polarization responses are listed in Table 1. The radar was assumed to operate at 2 GHz center frequency and have approximately 1 m $\times$ 0.96 m range$\times$cross-range resolution. PFA is used to generate initial images for each of $M = 4$ polarization channels. (For any radar, $M \leq 4$). The cross-channel contamination is generated with Gaussian random off-diagonal elements and is

$$\underline{\underline{\boldsymbol{C}}} = \begin{bmatrix} 1.0000 & 0.1065 & 0.0934 & 0.4287 \\ 0.3704 & 1.0000 & 0.4995 & 0.0536 \\ 0.2936 & 0.1253 & 1.0000 & 0.3782 \\ 0.1993 & 0.2099 & 0.1544 & 1.0000 \end{bmatrix}. \tag{14}$$

Physical antenna properties may induce more structure in $\underline{\underline{\boldsymbol{C}}}$ in practice but the random case provides an illustrative example. For now it is assumed that we can know $\underline{\underline{\boldsymbol{C}}}$ via radar calibration. Complex white Gaussian noise is added to the contaminated images with a peak signal-to-noise ratio (SNR) of 30 dB. The PFA and noisy, crosstalk contaminated images are shown in Figure 1. Circles indicate a target location and are displayed for reference in all image channels regardless of target polarization type.

Following the approach discussed in Section 4, we solve (10) and (11) with $p = 1$ and $\lambda_1 = 0.4$, $\lambda_2 = 0.3$ to enhance point features in each image. Figures 2 and 3 show the sparse images recovered in each case. Figures 1-3 are all plotted according to the dynamic range shown in the colorbar in Figure 1. Values of λ_1 and λ_2 are chosen arbitrarily to yield similar visual sparsity. As desired, noise, cross-channel contamination, and point spreading are reduced in both sparse solutions.

A CMY color representation of the sparse-regularization results is shown in Figure 4. The CMY representation does not appear sparse like Figures 2 and 3 since only polarization (not amplitude) information is displayed. The CMY coefficients for each target pixel are listed in the image. The total absolute error (TAE) between the computed and ideal CMY values (computed as $|\hat{C} - C| + |\hat{M} - M| + |\hat{Y} - Y|$ for each target pixel) is listed in Table 1. Solutions to both (10) and (11) recover estimates of the desired polarimetric signatures for each target pixel that reduce CMY error compared to the observed images. However, the TAE values for (10) and (11) should not be directly compared since, as noted in Section 4, the two problems are not equivalent. Rather, the TAE values serve to show that each approach provides a valid sparse multi-channel enhancement that estimates the true target polarization responses, resulting in purer CMY colors for Targets 1, 2, and 3. Target 4 contains three point scatterers of equal proportion, each with a different polarization type. The jointly-enhanced images have a better balance of colors (scatterer proportion) than the observed contaminated, noisy images, providing more accurate overall target information than the initial images.

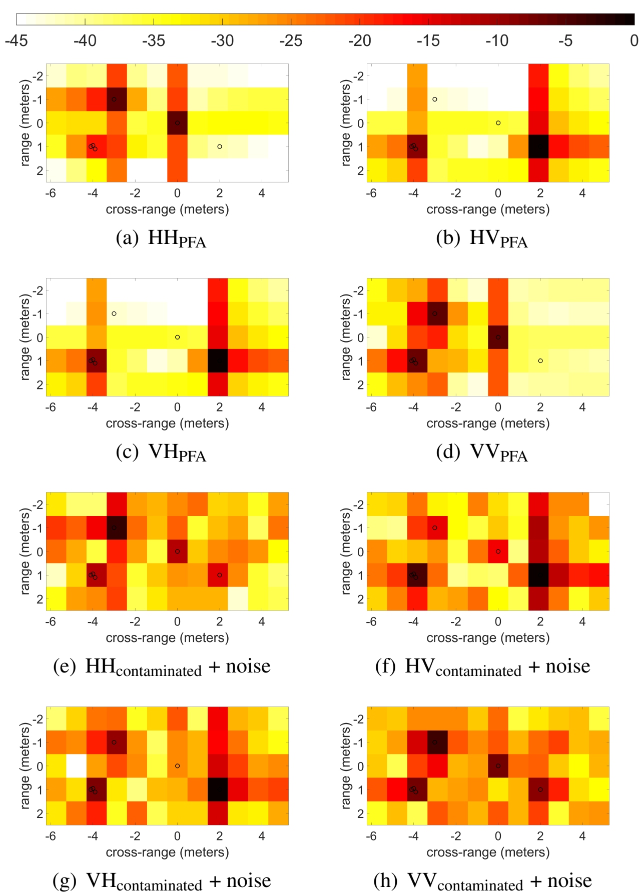

Fig. 1. Original PFA images and observed noisy, crosstalk contaminated images. (Colorbar units are dBsm.)

Table 1. Ideal target truth and estimated target reflectivity CMY polarization coefficient errors.

	Scatterer Location (range,cross-range) meters	Scatterer Amplitude	Scatterer Polarization Type	Ideal Pol. Response [HH,HV,VH,VV]	Ideal [C,M,Y] Target Pixel Coefficients	CMY Total Absolute Error: PFA Image	Observed Images	Sparse Decoupling (Solution to (10))	Pre-processed (Solution to (11))
Target 1	$(-1,-3)$	1	trihedral	$\frac{1}{\sqrt{2}}[1,0,0,1]$	$[1,0,0]$	0.0357	0.5075	0.1185	0.0992
Target 2	$(0,0)$	1	dihedral	$\frac{1}{\sqrt{2}}[1,0,0,-1]$	$[0,1,0]$	0.0404	0.4323	0.0933	0.0298
Target 3	$(1,2)$	2	cross-pol	$\frac{1}{\sqrt{2}}[0,1,1,0]$	$[0,0,1]$	0.0126	0.3091	0.0013	0.0020
Target 4	$(0.95,-4)$ $(1,-4.1)$ $(1.1,-3.9)$	0.5 0.5 0.75	trihedral dihedral cross-pol	$\frac{1}{\sqrt{2}}[1,0,0,1]$ $\frac{1}{\sqrt{2}}[1,0,0,-1]$ $\frac{1}{\sqrt{2}}[0,1,1,0]$	$\begin{bmatrix}0.4851\\0.4851\\0.7276\end{bmatrix}^T$	0.0587	0.4190	0.2806	0.1430

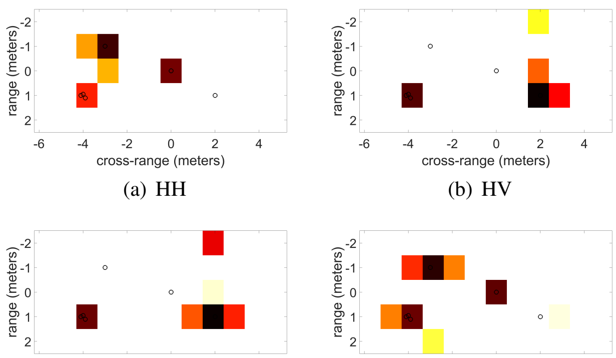

(a) HH (b) HV (c) VH (d) VV

Fig. 2. Multi-channel sparse regularization image enhancement results. (Solution to (10) for $\lambda_1 = 0.4$).

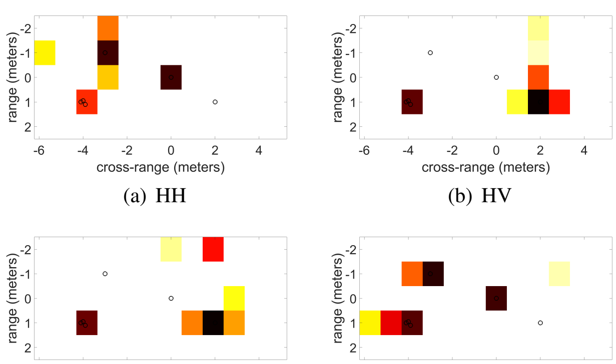

(a) HH (b) HV (c) VH (d) VV

Fig. 3. Multi-channel sparse regularization image enhancement results for decoupled data. (Solution to (11) for $\lambda_2 = 0.3$).

6. CONCLUSION

We extended sparsity-regularized SAR imaging to recover canonical scattering signatures from crosstalk-contaminated polarimetric radar data. Incorporation of crosstalk in the multi-channel sparse optimization allows for future exploitation of the proposed framework to study interesting cases of non-invertible or unknown crosstalk. An initial study into polarimetric radar compressive sensing by dropping a channel (i.e. a row of $\underline{\underline{C}}$) is underway [27].

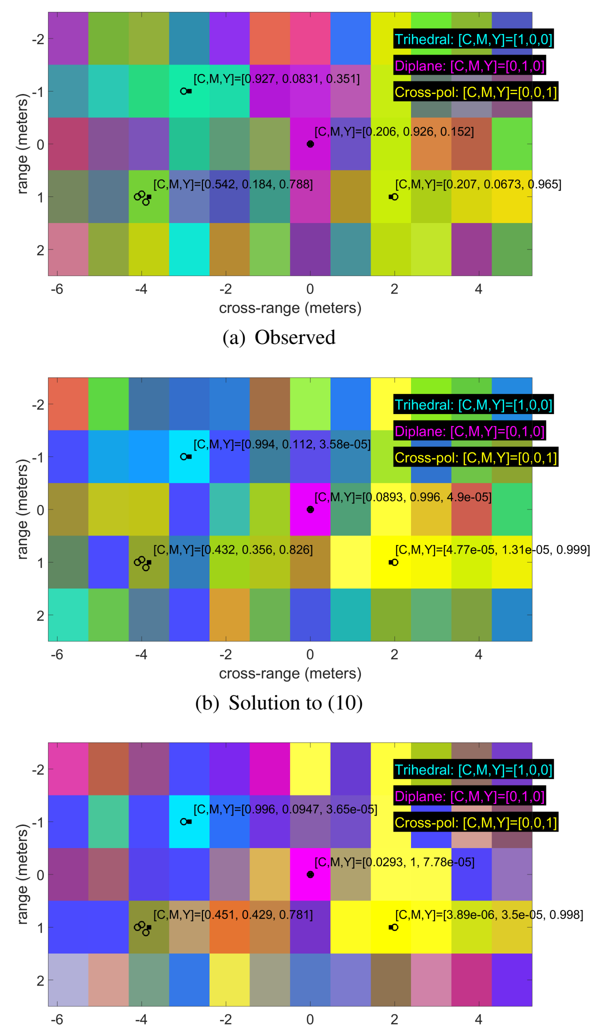

(a) Observed

(b) Solution to (10)

(c) Solution to (11)

Fig. 4. Pseudocolor polarimetric results showing recovery of target pixel polarization signatures.

7. REFERENCES

[1] M. Cetin and W. C. Karl, "Feature-enhanced synthetic aperture radar image formation based on nonquadratic regularization," *IEEE Transactions on Image Processing*, vol. 1, no. 4, pp. 623–

631, April 2001.

[2] T. Kragh and A. Kharbouch, “Monotonic iterative algorithms for SAR image restoration,” in *IEEE International Conference on Image Processing*, 2006, pp. 645–648.

[3] D. L. Donoho, M. Elad, and V. N. Temlyakov, “Stable recovery of sparse overcomplete representations in the presence of noise,” *IEEE Transactions on Information Theory*, vol. 52, no. 1, Jan. 2006.

[4] R. Baraniuk, “Compressive sensing [lecture notes],” *IEEE Signal Processing Magazine*, vol. 24, no. 4, pp. 118–121, July 2007.

[5] M. Cetin, I. Stojanovic, N. O. Onhon, K. R. Varshney, S. Samadi, W. C. Karl, and A. S. Willsky, “Sparsity-driven synthetic aperture radar imaging,” *IEEE Signal Processing Magazine*, pp. 27–40, July 2014.

[6] C. D. Austin, E. Ertin, and R. L. Moses, “Sparse multipass 3D SAR imaging: applications to the GOTCHA data set,” in *Proc. SPIE*, 2009, vol. 7337, pp. 733703–733703–12.

[7] M. Ferrara, J. A. Jackson, and C. Austin, “Enhancement of multi-pass 3D circular SAR images using sparse reconstruction techniques,” in *Proc. SPIE*, 2009, vol. 7337, pp. 733702–733702–10.

[8] J. A. Jackson and R. L. Moses, “Synthetic aperture radar 3D feature extraction for arbitrary flight paths,” *IEEE Transactions on Aerospace and Electronic Systems*, vol. 48, no. 3, pp. 2065–2084, July 2012.

[9] N. Ramakrishnan, E. Ertin, and R. L. Moses, “Enhancement of coupled multichannel images using sparsity constraints,” *IEEE Transactions on Image Processing*, vol. 19, no. 8, pp. 2115–2136, Aug 2010.

[10] S. Samadi, M. Cetin, and M. A. Masnadi-Shirazi, “Sparse representation-based synthetic aperture radar imaging,” *IET Radar, Sonar Navigation*, vol. 5, no. 2, pp. 182–193, Feb 2011.

[11] S. Samadi, M. Cetin, and M. A. Masnadi-Shirazi, “Multiple feature-enhanced SAR imaging using sparsity in combined dictionaries,” *IEEE Geoscience and Remote Sensing Letters*, vol. 10, no. 4, pp. 821–825, July 2013.

[12] K. R. Varshney, M. Cetin, J. W. Fisher, III, and A. S. Willsky, “Sparse representation in structured dictionaries with application to synthetic aperture radar,” *IEEE Transactions on Signal Processing*, vol. 56, no. 8, pp. 3548–3561, Aug. 2008.

[13] G. B. Hammond and J. A. Jackson, “SAR canonical feature extraction using molecule dictionaries,” in *IEEE Radar Conference*, April 2013, pp. 1–6.

[14] L. Zhang, L. Sun, B. Zou, and W. M. Moon, “Fully polarimetric SAR image classification via sparse representation and polarimetric features,” *IEEE Journal of Selected Topics in Applied Earth Observations and Remote Sensing*, vol. 8, no. 8, pp. 3923–3932, Aug. 2015.

[15] M. A. Saville, J. A. Jackson, and D. F. Fuller, “Rethinking vehicle classificatioin with wide-angle polarimetric SAR,” *IEEE Transactions on Aerospace and Electronic Systems*, vol. 29, no. 1, pp. 41–49, Jan. 2014.

[16] M. Amin, Ed., *Compressive Sensing for Urban Radar*, CRC Press, Boca Raton, FL, 2015.

[17] S. R. Cloude, *Polarisation: applications in remote sensing*, Oxford University Press, 2010.

[18] R. Touzi, P. W. Vachon, and J. Wolfe, “Requirement on antenna cross-polarization isolation for the operational use of c-band SAR constellations in maritime surveillance,” *IEEE Geoscience and Remote Sensing Letters*, vol. 7, no. 4, pp. 861–865, Oct 2010.

[19] K. Sarabandi, F. T. Ulaby, and M. A. Tassoudji, “Calibration of polarimetric radar systems with good polarization isolation,” *IEEE Transactions on Geoscience and Remote Sensing*, vol. 28, no. 1, pp. 70–75, Jan. 1990.

[20] C. V. Jakowatz, D. E. Wahl, P. H. Eichel, D. C. Ghiglia, and P. A. Thompson, *Spotlight-mode synthetic aperture radar : a signal processing approach*, Kluwer Academic Publishers, Boston, 1996.

[21] S. W. Chen, Y. Z. Li, X. S. Wang, S. P. Xiao, and M. Sato, “Modeling and interpretation of scattering mechanisms in polarimetric synthetic aperture radar: Advances and perspectives,” *IEEE Signal Processing Magazine*, vol. 31, no. 4, pp. 79–89, July 2014.

[22] W. L. Cameron and L. K. Leung, “Feature motivated polarization scattering matrix decomposition,” in *IEEE International Radar Conference*, 1990, pp. 549–557.

[23] S. R. Cloude and E. Pottier, “A review of target decomposition theorems in radar polarimetry,” *IEEE Transactions on Geoscience and Remote Sensing*, vol. 34, no. 2, pp. 498–518, March 1996.

[24] O. Batu and M. Cetin, “Parmater selection in sparsity-driven SAR imaging,” *IEEE Transactions on Aerospace and Electronic Systems*, vol. 47, no. 4, pp. 3040–3050, Oct. 2011.

[25] S. Ling and T. Strohmer, “Self-calibration and biconvex compressive sensing,” *Inverse Problems*, vol. 31, no. 11, pp. 115002, 2015.

[26] R. Barrett et al., *Templates for the Solution of Linear Systems: Building Blocks for Iterative Methods*, Society for Industrial and Applied Mathematics, 1993.

[27] J. A. Jackson and F. Lee-Elkin, “Channel crosstalk model for fully-polarimetric SAR compressive sensing,” in *submitted to IEEE Radar Conference*, May 2017.